Materials Advances

ROYAL SOCIETY OF CHEMISTRY

PAPER

View Article Online
View Journal | View Issue

Cite this: *Mater. Adv.*, 2026, 7, 597

Donor positional inversion in carbazole–cyanostilbene conjugates: reorienting connectivity for solid-state color modulation

A. Afrin, U. Adithyamol and P. Chinna Ayya Swamy *

Received 29th August 2025,
Accepted 12th November 2025

DOI: 10.1039/d5ma00978b

rsc.li/materials-advances

A donor–acceptor–donor (D–A–D) carbazole–cyanostilbene luminophore incorporating anthracene donors has been developed to probe the role of donor orientation on structure–property relationships. Compared with previously reported donor–donor–acceptor (D–D–A) analogues, the D–A–D architecture preserves absorption features but markedly alters emission behavior. While absorption spectra remain nearly solvent-independent, the emission undergoes a solvatochromic red-shift from 560 nm in hexane to 617 nm in DMF. In dichloromethane, the D–A–D system emits weakly at 575 nm, contrasting with the blue-green emission (468 nm) of the D–D–A analogue, underscoring the impact of donor inversion on excited-state relaxation. Aggregation studies reveal a combination of aggregation-induced emission (AIE) and aggregation-caused quenching (ACQ), with maximum fluorescence intensity observed at 50% water fraction, supported by SEM and DLS analysis of nano-assemblies. In the solid state, the luminophores display bright yellow emission ($\Phi \approx 52\%$) with reversible mechanochromic switching between crystalline and amorphous forms, as confirmed by PXRD. Thermal analysis demonstrates high stability (T_d = 361 °C; T_m = 206 °C). These results establish donor inversion as a powerful design strategy to tune color, enhance efficiency, and achieve stimuli-responsive luminescence in carbazole–cyanostilbene systems, offering a versatile platform for advanced solid-state emitters.

Introduction

The development of organic luminophores that retain high emissive efficiency in the solid state remains a central objective in materials chemistry, particularly for applications in organic light-emitting diodes (OLEDs),[1–5] sensing devices,[6–9] data storage,[10–12] and smart photonic materials.[13–15] A recurring challenge in this domain is aggregation-caused quenching (ACQ), where strong intermolecular π–π interactions in the condensed phase deactivate excited states non-radiatively. The counteracting concept of aggregation-induced emission (AIE) has emerged as a powerful strategy, in which restriction of intramolecular motion upon aggregation enhances luminescence intensity.[16,17] In addition to AIE, mechanochromism has also garnered considerable attention in the context of solid-state organic luminophores. Mechanochromic materials exhibit reversible changes in their optical properties, typically fluorescence color or intensity upon exposure to external stimuli such as grinding, pressing, or shearing. These transformations often arise from alterations in molecular packing, conformational reorganization, or phase transitions between crystalline and amorphous states.[18–20] Because of their responsiveness and reversibility, mechanochromic luminophores hold significant promise for applications in security inks,[21–23] sensors,[24,25] memory devices,[26–28] and rewritable data storage.[29–32] Incorporating mechanoresponsive behavior into AIE-active systems thus creates opportunities for multifunctional materials that combine robust solid-state emission with dynamic, stimulus-responsive properties.[33–35] Among various frameworks, cyanostilbene derivatives are particularly attractive due to their rigid, extended conjugation, facile functionalization, and ability to form twisted conformations that minimize π-stacking making them ideal candidates for solid-state emitters.[36–40]

In our previous study, we designed and synthesized a family of carbazole–anthracene–cyanostilbene conjugates constructed in a donor–donor–acceptor (D–D–A) fashion.[41] The incorporation of strong electron-donating groups (carbazole and anthracene) enabled effective modulation of the intramolecular charge transfer (ICT) process, leading to materials that not only showed efficient solid-state fluorescence and clear AIE behavior, but also displayed reversible mechanofluorochromism (MFC), where emission color could be reversibly altered by mechanical grinding and solvent fuming. These results highlighted how the interplay

Main group Organometallics Optoelectronic Materials and Catalysis lab, Department of Chemistry, National Institute of Technology, Calicut-673601, India. E-mail: swamy@nitc.ac.in

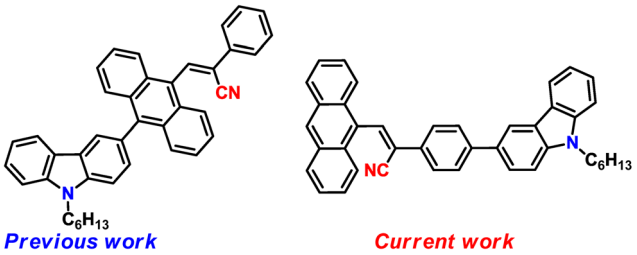

Chart 1 Molecular structure of isomers reported in previous work and current work.

between molecular design, electronic structure, and intermolecular interactions governs the photophysical behavior of organic luminophores. While the D–D–A motif proved effective, it also raised a deeper structural question: how does the positional arrangement of donor groups influence the overall photophysical profile? This fundamental query led us to pursue the design of a new class of molecules that retain the cyanostilbene core but undergo a donor positional inversion. In the current study, we report anthracene–cyanostilbene–carbazole conjugates, wherein the anthracene unit, previously central, is now located at the terminal position opposite to carbazole, forming a donor–acceptor–donor (D–A–D) topology. This positional inversion preserves donor strength and conjugation length, but alters the connectivity and symmetry of the system, offering a direct comparison with the earlier D–D–A analogues (Chart 1). Interestingly, our investigation revealed that while ICT modulation is similar to that of D–D–A, the D–A–D systems exhibit bright yellow emission in the solid state with a quantum yield of ~52%, a clear interplay between AIE and ACQ processes, and reversible MFC behavior. These findings highlight donor orientation as a subtle yet influential design parameter: rather than drastically altering charge transfer, it governs emission efficiency, aggregation pathways, and mechanochromic response. By isolating the effect of connectivity within a common molecular framework, this work provides new insights into the role of donor positioning in tuning photophysical properties, offering guidance for the rational design of responsive solid-state fluorophores.

Results and discussion

Synthesis and characterisation

The donor–acceptor–donor (D–A–D) anthracene–cyanostilbene–carbazole conjugates were synthesized *via* a Suzuki-cross-coupling reaction between (*Z*)-3-(anthracen-9-yl)-2-(4-bromophenyl)-acrylonitrile and carbazole boronic ester derivatives (Scheme 1). The reactions proceeded efficiently to afford the target isomer in moderate yields. The structure was fully characterized by ^{1}H and ^{13}C NMR and HRMS (Fig. S1–S3). This design represents a positional inversion compared to our previously reported D–D–A analogues.[41] While the molecular fragments remain identical, the donor connectivity is reversed, placing anthracene at the periphery opposite to carbazole. Such a rearrangement maintains donor strength and conjugation length but introduces a different symmetry in the π-framework, enabling a direct comparison of how donor orientation governs electronic structure and solid-state photophysics. Fortunately, we were able to obtain single crystals of **AN-CS-CZ** yellow crystals *via* slow evaporation of an acetonitrile solution at room temperature. The crystal structure of **AN-CS-CZ** was further elucidated *via* single-crystal X-ray diffraction (XRD) analysis, providing a definitive confirmation of its molecular architecture, as depicted in Fig. 1 and Table S1.

Single crystal structure analysis

Single crystals of **AN-CS-CZ** (D–A–D) suitable for X-ray diffraction were obtained by slow evaporation of its acetonitrile solution at room temperature, yielding yellow block-like crystals. The compound crystallizes in a monoclinic system with space group $P2_1/c$ (no. 14) and $Z = 4$, incorporating one acetonitrile molecule per asymmetric unit. The molecular structure was unambiguously confirmed, revealing the expected donor–acceptor–donor configuration, where anthracene units occupy termini of the conjugated cyanostilbene–carbazole backbone. The molecule adopts an overall twisted conformation, primarily due to steric interactions between the anthracene and cyanostilbene moieties. This geometric distortion limits direct π–π overlap, thereby suppressing aggregation-caused quenching (ACQ) and promoting efficient radiative decay consistent with

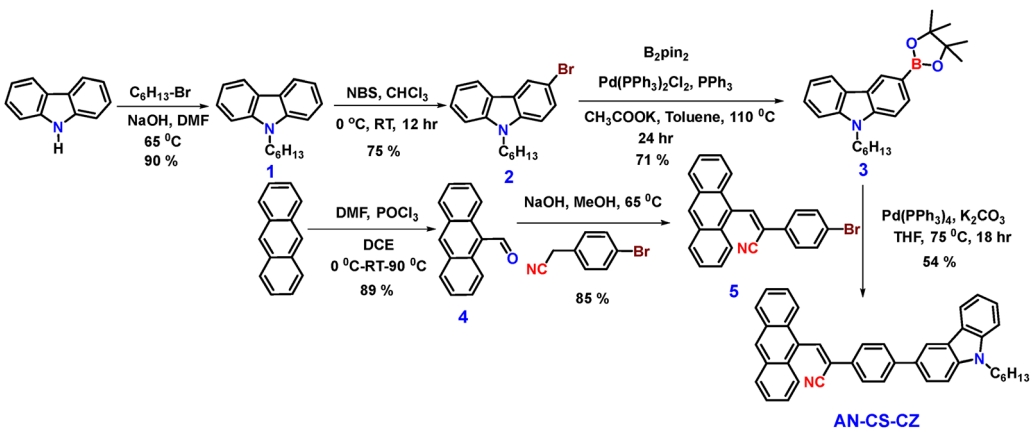

Scheme 1 Synthetic scheme for the target compound **AN-CZ-CS**.

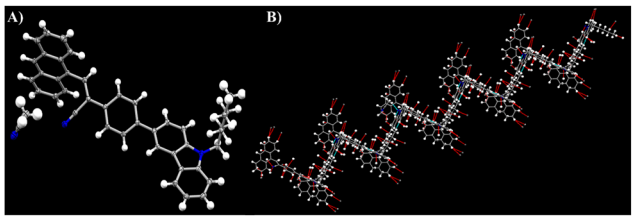

Fig. 1 (A) Crystal structure of compound **AN-CS-CZ** and (B) packing arrangement of the compound **AN-CZ-CS** viewed along the *b* axis.

the high solid-state quantum yield of the compound. The crystal packing diagram (Fig. 1B), viewed along the *b*-axis, reveals a zig-zag layered arrangement of **AN-CS-CZ** molecules propagating along the *a*-axis. The molecules stack in a slipped edge-to-face fashion, forming alternating layers. Such a zig-zag alignment between adjacent anthracene and carbazole units prevents complete cofacial overlap and enables short intermolecular contacts, including C–H···π (2.7–2.9 Å) and C–H···N (2.8 Å) interactions (Fig. S4 and S5). The π–π centroid separations (~3.20 Å) indicate a slipped stacking rather than direct planar overlap, consistent with the absence of strong excimer formation, efficiently minimizing nonradiative pathways. Weak C–H···π contacts (~2.8 Å) between adjacent aromatic planes further strengthen the three-dimensional lattice. The acetonitrile solvent molecules occupy interstitial voids and participate in C–H···N contacts, reinforcing the packing architecture without disturbing the conjugated framework. Overall, the zig-zag layered packing, combined with the twisted conformation and directional weak interactions, gives rise to a rigid, thermally stable, and highly emissive solid-state structure, in excellent agreement with the enhanced photoluminescence efficiency observed experimentally.

Photophysical properties in solution

The UV-vis absorption spectrum of **AN-CS-CZ** (Fig. 2) reveals multiple structured bands characteristic of the anthracene–cyanostilbene–carbazole framework. Intense absorptions in the 280–320 nm region originate from π–π* transitions of the carbazole and cyanostilbene units, while distinct features between

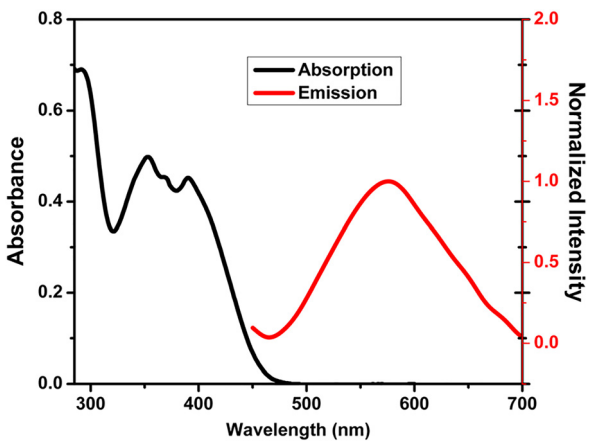

Fig. 2 Absorption and normalized emission spectra of the compound **AN-CS-CZ** in DCM solution (Con. 3×10^{-5} M; λ_{ex} = 385 nm).

340–390 nm correspond to the extended π-conjugation of the anthracene donor, overlapping with intramolecular charge-transfer (ICT) contributions.[42] Comparison with the previously reported D–D–A analogue shows that the overall spectral shapes are closely related, consistent with the identical conjugated fragments employed. However, subtle differences are evident: the D–A–D isomer exhibits relatively enhanced absorption in the 340–390 nm region, highlighting stronger participation of the terminal anthracene donor when directly coupled to the cyanostilbene core. In contrast, the D–D–A systems display more balanced absorption profiles, reflecting a more distributed donor contribution. Furthermore, on comparing the emission spectra, **AN-CS-CZ** conjugates exhibit distinctly red-shifted and weaker emission in solution compared to the previously reported D–D–A analogues. In dilute dichloromethane solution, the emission maximum appears at 575 nm with low intensity, whereas the earlier system emits at 468 nm. This marked bathochromic shift arises from enhanced donor–acceptor communication introduced by the positional inversion of anthracene and carbazole, which stabilizes the charge-transfer (CT) excited state but simultaneously opens non-radiative decay channels.

The solvent dependent studies further revealed polarity-dependent shifts. The UV-vis absorption spectra of **AN-CS-CZ** remained essentially unchanged across solvents of varying polarity, with the lowest-energy absorption band consistently centered around 390 nm (Fig. S6(A)). The absence of spectral shifts in absorption highlights that the ground-state electronic distribution is largely unaffected by solvent environment, consistent with a locally excited (LE) nature of the transition. Meanwhile, the emission maximum varied from 560 nm in nonpolar hexane to 617 nm in strongly polar DMF, corresponding to a red-shift of ~57 nm (Fig. S6(B) and Table S2). This substantial solvatochromic behavior indicates a strong intramolecular charge-transfer (ICT) character in the excited state, reflecting efficient donor–acceptor electronic communication through the conjugated cyanostilbene–carbazole bridge. The enhanced polarity of the excited state suggests significant stabilization in polar solvents. Thus, while the solution-state emission is dominated by an ICT state with reduced quantum yield due to nonradiative relaxation, the bright solid-state luminescence (*vide infra*) highlights the role of molecular restriction and packing in promoting radiative decay.

AIE *vs.* ACQ behavior

To probe aggregation effects, fluorescence measurements were carried out in acetonitrile/water mixtures with varying water fractions (f_w). In pure acetonitrile, the emission intensity was weak, consistent with active non-radiative decay in solution. Upon gradual addition of water, aggregation was induced due to the poor solubility of the luminophore in aqueous medium. A pronounced increase in emission intensity was observed when f_w exceeded 30%, reaching a maximum at 50% water content (Fig. 3). This enhancement is attributed to restriction of intramolecular motion (RIM) in the aggregated state, which effectively suppresses non-radiative decay pathways. At higher water fractions (>50%), the emission intensity decreased,

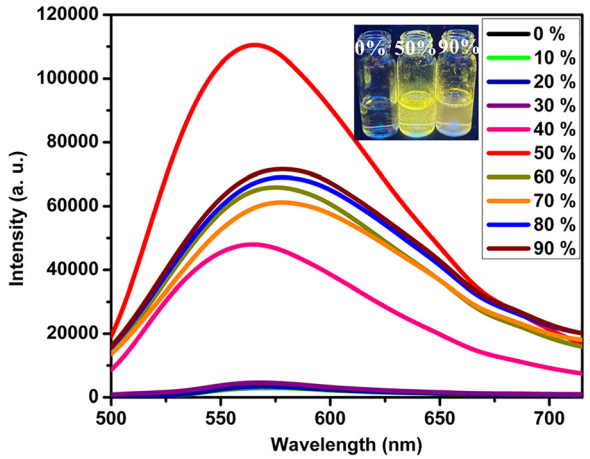

Fig. 3 Emission spectra of **AN-CS-CZ** in ACN/water mixtures with different f_w (Con. 3×10^{-5} M; λ_{ex} = 385 nm). The inset contains digital photos taken under a UV 365 nm lamp.

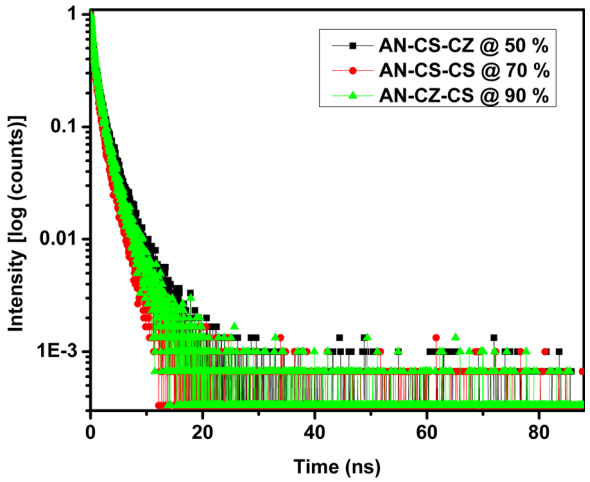

Fig. 4 Lifetime profiles for the **AN-CS-CZ** at different fractions of water.

reflecting the onset of aggregation-caused quenching (ACQ). Thus, **AN-CS-CZ** exhibits a clear AIE–ACQ interplay, where radiative decay is enhanced in packed aggregates but quenched due to the dissolution of aggregates, in contrast to our previously reported typical D–D–A AIEgen. The aggregation morphology was further examined by scanning electron microscopy (SEM) at 50% f_w, where emission was most intense. The SEM images revealed the formation of well-defined ordered nanostructures, consistent with efficient RIM and enhanced fluorescence (Fig. S7). Complementary dynamic light scattering (DLS) measurements supported these observations, giving a particle size of 232 nm at 50% water fraction, which decreased to ~60 nm in 90% water fraction (Fig. S8). These results confirm that the photophysical behavior is closely correlated with aggregate size and packing mode, highlighting the sensitivity of the D–A–D system to aggregation conditions.[43]

To gain deeper insight into the aggregation-induced emission (AIE) and aggregation-caused quenching (ACQ) behavior of the D–A–D conjugates, we conducted time-correlated single-photon counting (TCSPC) measurements at water fractions (f_w) of 50%, 70%, and 90% (Fig. 4 and Table 1). The results reveal a clear correlation between the excited-state lifetimes and the observed steady-state fluorescence intensities, providing quantitative information about the radiative and non-radiative decay processes in different aggregation environments. At 50% water fraction, which corresponds to the maximum fluorescence intensity, the average excited-state lifetime is the longest, indicating efficient radiative decay. This suggests that the aggregates formed under these conditions are optimally packed, restricting intramolecular rotations and vibrations, which minimizes non-radiative pathways and enhances emission efficiency, consistent with classical AIE behavior. Upon increasing the water fraction to 70%, the average lifetime decreases to its lowest value, matching the observed drop in fluorescence intensity. This behavior indicates the onset of partial quenching, likely due to reorganization of aggregates, which promote non-radiative decay channels. At 90% water fraction, the lifetime increases relative to 70%, although it remains shorter than at 50%. This intermediate behavior aligns with the steady-state spectra, where the fluorescence intensity at 90% f_w is higher than at 70% suggesting that although some aggregates partially dissolve, a fraction of emissive aggregates persists, partially restoring radiative decay efficiency. These trends closely match the steady-state fluorescence data, where the intensity decreases in the order 50% > 70% > 90%. Overall, the TCSPC data clearly demonstrate that emission efficiency is strongly influenced by aggregate morphology and solvent environment. The combination of decreased lifetime at intermediate aggregation (70%) and partial recovery at high water content (90%) provides quantitative evidence of the delicate balance between AIE enhancement and ACQ suppression. These findings underscore the importance of solvent-induced aggregation control in tuning the photophysical properties of D–A–D conjugates and provide mechanistic insight into the relationship between aggregate structure and excited-state dynamics in solution–water mixtures.

Table 1 Life time parameters of the compounds in aggregated states

Compounds	τ_1 (ns)	τ_2 (ns)	τ_3 (ns)	A_1	A_2	A_3	τ_{avr}	χ^2
AN-CS-CZ (50%)	0.95	2.75	0.23	35.52	46.94	17.53	**1.66**	1.13
AN-CS-CZ (70%)	0.82	2.36	0.23	42.90	35.42	21.68	**1.23**	1.06
AN-CS-CZ (90%)	0.95	2.75	0.23	47.83	36.12	16.05	**1.48**	1.18

τ_{avr} is calculated using the formula $\tau_{avr} = \frac{\sum(A_n\tau_n)}{\sum(A_n)}$. A is the percentage fraction of each life time component τ.

Solid-state emission and mechanochromism

In the solid state, the D–A–D luminophores exhibited bright yellow fluorescence with emission maxima at 560 nm and absolute solid-state quantum yields of ~52% (Table 2). This is a notable shift compared to the previously reported D–D–A analogues, which emitted in the green region (520 nm) with slightly lower efficiencies (22%). The red-shift to yellow suggests that donor orientation impacts packing-induced stabilization of the excited state, favoring lower-energy emission. The solid powders displayed reversible mechanochromic luminescence. The pristine samples showed yellow emission at 560 nm, which shifted to 585 nm upon mechanical grinding, accompanied by an obvious color change under UV light (Fig. 5(A)). Exposure of the ground powders to solvent vapors (*e.g.*, dichloromethane) restored the original emission profile, demonstrating reversible mechanochromism, with the recyclability remaining stable over more than five cycles (Fig. 5(C)). Powder X-ray diffraction (PXRD) analysis provided insight into this transformation: sharp crystalline peaks in the pristine state became diffuse upon grinding, indicating amorphization, and reappeared after fuming >5 cycles (Fig. 5(B)). These results confirm that the mechanochromism originates from packing rearrangements between crystalline and amorphous states, consistent with other cyanostilbene-based AIEgens.[44] Importantly, the persistence of reversible MFC in the D–A–D systems underscores the robustness of this behavior, regardless of donor position.

To correlate the molecular arrangement with thermal stability and solid-state emissive properties, variable-temperature powder X-ray diffraction (V-PXRD) measurements were performed for both the D–D–A and D–A–D conjugates in the range of 27–180 °C (Fig. S9). For the D–D–A compound, the diffraction pattern at room temperature shows slightly less intense peaks on compared with the same one under heating. Upon gradual heating to 100 °C and 180 °C, the diffraction peaks become sharper and more intense, signifying a thermally induced enhancement in crystallinity maybe due to the molecular planarization and improved π–π interactions. After cooling to room temperature, the sharper reflections remain, confirming that the heat-driven structural ordering is largely reversible and thermally stable. This reversible enhancement in order explains the consistent emission color but moderate fluorescence intensity, as excessive π–π stacking in the highly ordered phase can facilitate nonradiative pathways through exciton migration.[45] Meanwhile, the D–A–D analogue (Fig. S9(B)) exhibits the same intense peaks throughout all the temperatures and upon cooling, the diffraction features recover fully. The D–A–D compound displays higher solid-state fluorescence quantum yield, implying that molecular packing is actually more favorable for radiative decay by minimizing aggregation-caused quenching (ACQ) and reducing excitonic coupling as evidenced from their crystal structure.

Table 2 Emission wavelengths of the compounds in DCM solution and the solid-state under various external stimuli and their absolute quantum yields

	Emission					
Compounds	Solution	Pristine	Ground	Fumed	Φ^a (%)	Φ^b (%)
AN-CS-CZ	575	560	585	565	0.8	52.3
DDA[41]	468	520	596	520	4	22

[a] Absolute quantum yield in solution. [b] Absolute quantum yield in solid-state in the pristine state. Wavelength in nm.

Theoretical calculations

To gain further insight into the electronic structure of the luminophore, density functional theory (DFT) studies were carried out. Geometry optimizations were performed at the B3LYP/6-31G(d,p) level of theory in the gas phase.[46] The optimized ground-state geometries reveal that the conjugates adopt a twisted configuration between the anthracene donor and the cyanostilbene acceptor core, which effectively suppresses extended π–π stacking and supports the observed solid-state emissive behavior. The degree of twisting is more pronounced in the donor-inverted architecture, emphasizing the role of molecular connectivity in modulating conjugation and electronic communication. Frontier molecular orbital (FMO) analysis shows that the HOMO is predominantly delocalized over the anthracene–cyanostilbene backbone together with the carbazole donor (excluding alkyl aparts), whereas the LUMO is mainly localized on the anthracene–cyanostilbene acceptor fragment (Fig. 6). This spatial separation of electron density suggests a donor–acceptor charge-transfer (CT) character, which is consistent with the experimentally observed solvatochromic emission. The calculated HOMO–LUMO energy gaps also show good correlation with the experimental absorption onsets. Overall, the computational findings provide a molecular-level rationale for the observed photophysical properties: (i) the twisted conformations suppress aggregation-caused quenching (ACQ), (ii) the separated HOMO/LUMO distributions promote CT emission, and (iii) positional inversion of donors fine-tunes the electronic landscape to achieve solid-state color modulation.

Thermal properties

The thermal stability of the D–A–D luminophore was evaluated by thermogravimetric analysis (TGA) and differential scanning calorimetry (DSC). The compound exhibited a high decomposition temperature (T_d = 361 °C, 5% weight loss), indicating excellent stability suitable for optoelectronic applications (Fig. S10). The DSC trace revealed a sharp endothermic transition corresponding to a melting point of 206 °C, which is essentially identical to that of the previously reported D–D–A analogue. This suggests that despite the inversion of donor positions, the overall crystal lattice energetics remain conserved. Together, the high T_d and reproducible melting point demonstrate that donor orientation alters the electronic and photophysical behavior without compromising intrinsic thermal robustness, underscoring the practical stability of these systems.

Organic photoluminescent materials and device relevance

To comprehensively evaluate the emissive characteristics of the D–A–D conjugates under device-relevant conditions, thin film

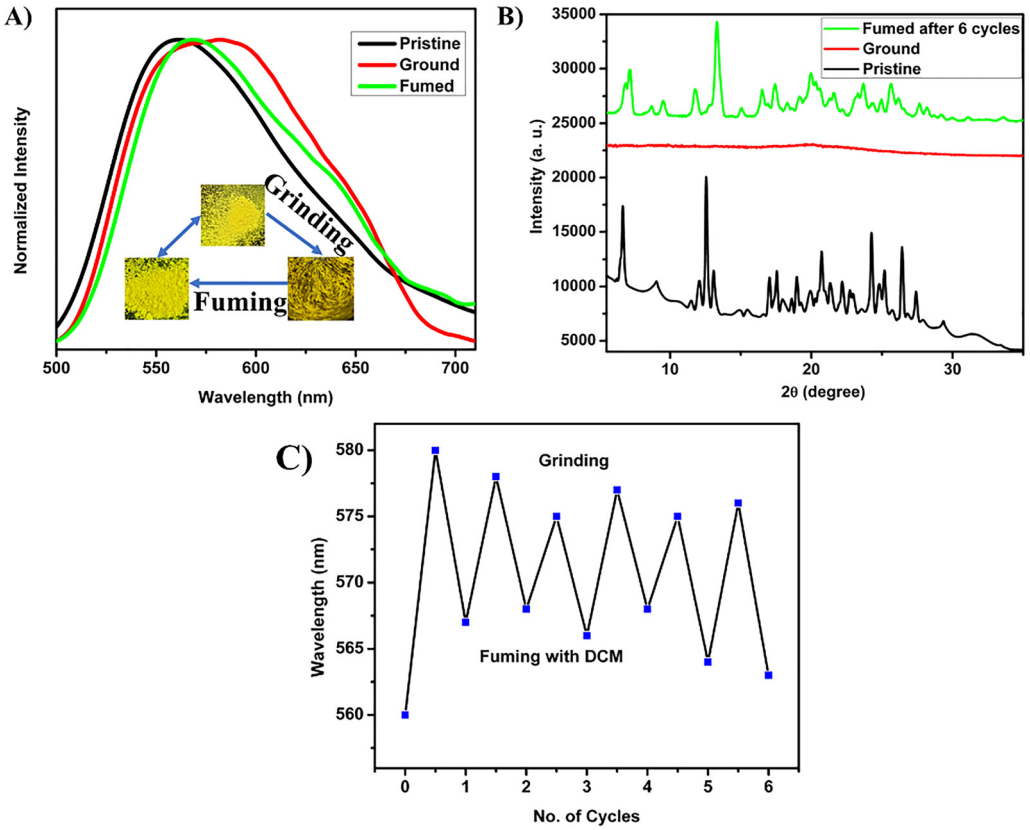

Fig. 5 (A) Normalized emission spectra of **AN-CS-CS** in the pristine state, after mechanical grinding, and following solvent fuming. The inset displays the corresponding photographs under 365 nm UV illumination. (B) Powder X-ray diffraction (PXRD) patterns of **AN-CS-CS** in different states and (C) reversibility plot of **AN-CZ-CS** after undergoing MFC for >5 cycles.

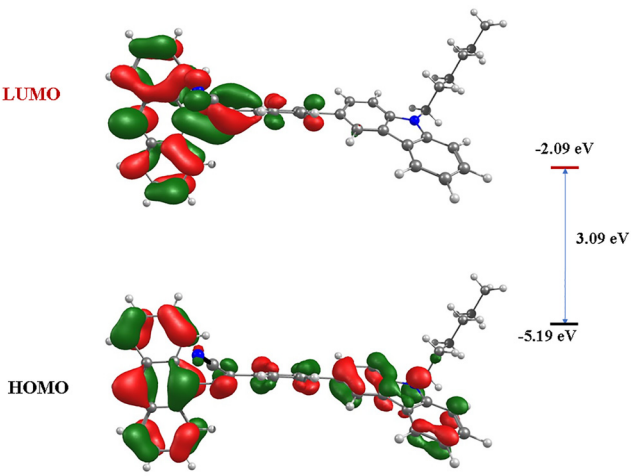

Fig. 6 FMO analysis of compound **AN-CS-CZ** and calculated energy gap.

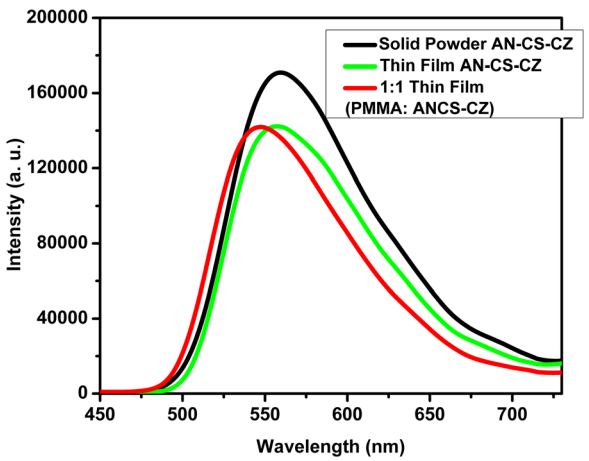

Fig. 7 Fluorescence spectra of **AN-CS-CZ**: powdered sample (black), drop-cast thin film (green), and 1:1 PMMA-compound film (red). All spectra were recorded with identical excitation and instrument settings.

emission studies were done by dropcasting $CHCl_3$ solutions of the compound onto clean quartz substrates (Fig. 7). The resulting films were uniform and transparent, exhibiting intense fluorescence with emission maxima nearly identical to that of the pristine solid powder. This close resemblance indicates that the emissive properties of the molecule are largely preserved upon film formation, suggesting that the radiative decay process is not strongly perturbed by the morphological change from a crystalline solid to an amorphous thin film. The thin films also displayed stable and reproducible fluorescence upon repeated excitation, confirming their good photostability. To further examine the influence of matrix dispersion on emission behavior, a 1:1 (w/w) PMMA-

compound composite film was prepared by co-dissolving the compound **AN-CS-CZ** and PMMA in $CHCl_3$ followed by drop-casting. The PMMA-embedded film exhibited slightly blue-shifted emission relative to both the pure film and the solid powder, consistent with partial restriction of molecular packing and reduced intermolecular interactions within the polymer matrix. The fluorescence intensity of the PMMA composite was also similar to the pure thin film and the film showed excellent optical homogeneity and transparency. This suggests that the luminophore is molecularly well-dispersed within the polymer host, minimizing aggregation-caused quenching (ACQ) while maintaining significant emissive strength. Importantly, the recovery of emission in such films highlights the emitter's excellent compatibility with polymeric hosts, reinforcing its potential for use in solid-state lighting and display applications.

In a broader context, organic photoluminescent materials such as these D–A–D conjugates possess intrinsic design flexibility and functional advantages that make them attractive for optical and optoelectronic integration.[47] Their emission color, charge-transfer (CT) characteristics, and efficiency can be systematically tuned through molecular engineering by adjusting donor/acceptor strength, π-spacer length, or substitution patterns to achieve the desired photophysical properties. Furthermore, their inherent solution processability allows low-cost and scalable fabrication of uniform films by spin-coating, drop-casting techniques. The mechanical flexibility, low density, and chemical tunability of such materials make them particularly suitable for next-generation, lightweight, and flexible devices. However, certain challenges persist, including sensitivity to moisture and oxygen, moderate thermal endurance relative to inorganic phosphors, and potential ACQ effects in densely packed states. These limitations can be effectively mitigated through rational AIE-based molecular design or host-matrix modulation, as demonstrated by the strong emission retention observed in the PMMA composite films. Although in-house OLED fabrication is currently unavailable in our laboratory, the consistent emission features observed in both thin-film and PMMA-compound samples confirm that the emissive characteristics of the D–A–D conjugates are stable across morphological variations. Together with their high solid-state luminescence, excellent thermal stability ($T_d \approx 361$ °C, $T_m \approx 206$ °C), and balanced frontier molecular orbital levels suitable for charge transport, these results strongly support the potential of these D–A–D systems for incorporation into organic light-emitting and photonic devices. The present findings thus provide a foundational understanding of their film-state photophysics and highlight their promise for future device integration once advanced fabrication facilities are available.

Conclusions

In summary, our study demonstrates that positional inversion of donor units in carbazole–cyanostilbene conjugates offers a powerful strategy to engineer photophysical properties while retaining excellent thermal stability. The D–A–D architecture not only preserves key absorption characteristics but also induces red-shifted emission, pronounced solvatochromism, and aggregation-induced emission (AIE) *vs.* ACQ behavior, making these systems highly tunable. Solid-state measurements reveal bright yellow emission with significantly enhanced quantum yields compared to previously reported D–D–A analogues, highlighting the critical role of donor orientation in governing excited-state dynamics. The observed reversible mechanochromic fluorescence (MFC) underscores the dynamic and stimuli-responsive nature of these materials, indicating their promise for next-generation optical sensors and smart photonic devices. Importantly, the robust thermal stability of these conjugates, together with their demonstrated bright and uniform thin-film emission, confirms their suitability for integration into OLED architectures and other flexible optoelectronic platforms. While we have not performed device fabrication in this study, the favorable photophysical and thermal properties, combined with tunable emission and reversible solid-state behavior, strongly indicate their suitability for practical applications. Taken together, these results provide actionable insights for rational design of advanced solid-state luminophores, demonstrating that simple structural reordering of donor fragments can unlock new emission colors, enhance device-relevant properties, and enable functional materials for real-world optoelectronic and photonic applications.

Author contributions

A. A. – conceptualization, data curation, formal analysis, investigation, methodology, validation, visualization, and writing – original draft. A. U. – methodology. C. A. S. P. – project administration, resources, supervision, validation, visualization, and writing – review and editing.

Conflicts of interest

The authors declare no competing financial interest.

Data availability

The data underlying this study are available in the published article and its supplementary information (SI). Supplementary information: ^{1}H NMR, ^{13}C NMR, HRMS, SCXRD and characterization data for the compound, photophysical data, SEM, DLS, and DFT results (PDF). See DOI: **https://doi.org/10.1039/d5ma00978b**.

CCDC 2500771 contains the supplementary crystallographic data for this paper.[48]

Acknowledgements

CAS P thanks, SERB/EEQ/2021/000180 for funding and support. A. A thanks the National Institute of Technology, Calicut, for the GATE-SRF fellowship. The authors acknowledge the Centre

for Materials Characterisation NIT Calicut for NMR and HRMS (DST-FIST), and Centre for Computational Modelling and Simulations NIT Calicut and Dept of Physics, NITC for the PXRD facility. We would like to thank the SEM Centre, the Department of Materials Science and Engineering, National Institute of Technology Calicut for the SEM facility. We would like to extend our sincere thanks to CIF IISER Trivandrum for the SCXRD facility.

References

1 J. Bauri, R. B. Choudhary and G. Mandal, Recent advances in efficient emissive materials-based OLED applications: a review, *J. Mater. Sci.*, 2021, **56**, 18837.
2 S. J. Zou, Y. Shen, F. M. Xie, J. D. Chen, Y. Q. Li and J. X. Tang, Recent advances in organic light-emitting diodes: toward smart lighting and displays, *Mater. Chem. Front.*, 2020, **4**, 788.
3 A. Salehi, X. Fu, D. H. Shin and F. So, Recent advances in OLED optical design, *Adv. Funct. Mater.*, 2019, **29**, 1808803.
4 M. K. Bera, P. Pal and S. Malik, Solid-state emissive organic chromophores: design, strategy and building blocks, *J. Mater. Chem. C*, 2020, **8**, 788–802.
5 X. Wu, S. Ni, C. H. Wang, W. Zhu and P. T. Chou, Comprehensive Review on the Structural Diversity and Versatility of Multi-Resonance Fluorescence Emitters: Advance, Challenges, and Prospects toward OLEDs, *Chem. Rev.*, 2025, **125**, 6685–6752.
6 L. Basabe-Desmonts, D. N. Reinhoudt and M. CregoCalama, Design of fluorescent materials for chemical sensing, *Chem. Soc. Rev.*, 2007, **36**, 993–1017.
7 L. Hu, Q. Zhang, X. Li and M. J. Serpe, Stimuli-responsive polymers for sensing and actuation, *Mater. Horiz.*, 2019, **6**, 1774–1793.
8 S. Jaiswal, S. Das, S. Kundu, I. Rawal, P. Anand and A. Patra, Progress and perspectives: fluorescent to long-lived emissive multifunctional probes for intracellular sensing and imaging, *J. Mater. Chem. C*, 2022, **10**, 6141.
9 M. Gao and B. Z. Tang, Fluorescent sensors based on aggregation-induced emission: recent advances and perspectives, *ACS Sens.*, 2017, **2**, 1382.
10 J. Q. Yang, Y. Zhou and S. T. Han, Functional applications of future data storage devices, *Adv. Electron. Mater.*, 2021, **7**, 2001181.
11 S. K. Patra, R. Manivannan and Y. A. Son, Multicolor emissive organic material to display aggregation caused red shift with dual state emission, and application towards rewritable data storage, *J. Photochem. Photobiol., A*, 2023, **444**, 114945.
12 D. Wu, W. Gong, H. Yao, L. Huang, Z. Lin and Q. Ling, Highly efficient solid-state emission of diphenylfumaronitriles with full-color AIE, and application in explosive sensing, data storage and WLEDs, *Dyes Pigm.*, 2020, **172**, 107829.
13 S. Ban, H. Yi, J. Park, Y. Huang, K. J. Yu and W. H. Yeo, Advances in Photonic Materials and Integrated Devices for Smart and Digital Healthcare: Bridging the Gap Between Materials and Systems, *Adv. Mater.*, 2025, 2416899.
14 M. Su and Y. Song, Printable smart materials and devices: strategies and applications, *Chem. Rev.*, 2021, **122**, 5144–5164.
15 A. M. Al-Amri, Recent progress in printed photonic devices: a brief review of materials, devices, and applications, *Polymers*, 2023, **15**, 3234.
16 J. Luo, Z. Xie, J. W. Lam, L. Cheng, H. Chen, C. Qiu, H. S. Kwok, X. Zhan, Y. Liu, D. Zhu and B. Z. Tang, Aggregation-induced emission of 1-methyl-1,2,3,4,5-pentaphenylsilole, *Chem. Commun.*, 2001, 1740.
17 J. Mei, N. L. C. Leung, R. T. K. Kwok, J. W. Y. Lam and B. Z. Tang, Aggregation-Induced Emission: Together We Shine, United We Soar!, *Chem. Rev.*, 2015, **115**, 11718–11940.
18 Y. Sun, Z. Lei and H. Ma, Twisted aggregation-induced emission luminogens (AIEgens) contribute to mechanochromism materials: a review, *J. Mater. Chem. C*, 2022, **10**, 14834–14867.
19 Z. Chi, X. Zhang, B. Xu, X. Zhou, C. Ma, Y. Zhang, S. Liu and J. Xu, Recent advances in organic mechanofluorochromic materials, *Chem. Soc. Rev.*, 2012, **41**, 3878–3896.
20 R. Misra, R. Gavale and F. Khan, Polymorphism in mechanochromic luminogens: recent advances and perspectives, *J. Mater. Chem. C*, 2025, **13**, 1063–1129.
21 Y. Hu, C. Qi, D. Ma, D. Yang and S. Huang, Multicolor recordable and erasable photonic crystals based on on-off thermoswitchable mechanochromism toward inkless rewritable paper, *Nat. Commun.*, 2024, **15**, 5643.
22 J. Sun, J. Han, Y. Liu, Y. Duan, T. Han and J. Yuan, Mechanochromic luminogen with aggregation-induced emission: implications for ink-free rewritable paper with high fatigue resistance and low toxicity, *J. Mater. Chem. C*, 2016, **4**, 8276–8283.
23 P. Shi, D. Deng, C. He, L. Ji, Y. Duan, T. Han, B. Suo and W. Zou, Mechanochromic luminescent materials with aggregation-induced emission: mechanism study and application for pressure measuring and mechanical printing, *Dyes Pigm.*, 2020, **173**, 107884.
24 P. Shi, Y. Duan, W. Wei, Z. Xu, Z. Li and T. Han, A turn-on type mechanochromic fluorescent material based on defect-induced emission: implication for pressure sensing and mechanical printing, *J. Mater. Chem. C*, 2018, **6**, 2476–2482.
25 J. Chen, L. Xu, M. Yang, X. Chen, X. Chen and W. Hong, Highly stretchable photonic crystal hydrogels for a sensitive mechanochromic sensor and direct ink writing, *Chem. Mater.*, 2019, **31**, 8918–8926.
26 M. I. Khazi, W. Jeong and J. M. Kim, Functional materials and systems for rewritable paper, *Adv. Mater.*, 2018, **30**, 1705310.
27 R. S. Bhagya, D. Sunil, K. Muthamma, P. Shetty and S. D. Kulkarni, Water-based invisible green flexographic ink for anti-counterfeit applications, *Prog. Org. Coat.*, 2022, **173**, 107212.
28 Y. Yang, Y. Chen, Y. Li, Z. Wang and H. Zhao, Acid-, mechano-and photochromic molecular switches based on a spiropyran derivative for rewritable papers, *Mater. Chem. Front.*, 2022, **6**, 916–923.

29 M. I. Khazi, W. Jeong and J. M. Kim, Functional materials and systems for rewritable paper, *Adv. Mater.*, 2018, **30**, 1705310.
30 X. M. Cai, Z. Tang, X. Chen, Y. Lin, X. Zhang and S. Huang, Construction of two rosin-based BioAIEgens with distinct fluorescence and mechanochromic propertites for rewritable paper, *Dyes Pigm.*, 2022, **204**, 110454.
31 H. Zhou, X. Du, J. Zhen, J. Long, X. Zhao and Q. Wang, Reversible mechanofluorochromic luminescence behaviors of triphenylamine-based compounds and their application in erasable writing, *J. Lumin.*, 2023, **263**, 120145.
32 B. Fang, M. Fan, H. Gao, Y. Wang, D. Gao, J. Yu, M. Yin and Y. Dai, A planar rigid steric group-modified spiropyran derivative with photochromism and mechanochromism for optical printing applications, *J. Mater. Chem. C*, 2024, **12**, 14361–14367.
33 J. He, Y. Yang, Y. Li, Z. He, Y. Chen, Z. Wang, H. Zhao and G. Jiang, Multiple anti-counterfeiting guarantees from simple spiropyran derivatives with solid photochromism and mechanochromism, *Cell Rep. Phys. Sci.*, 2021, **2**, 100643.
34 Q. Xia, W. Xie, T. He, H. Zhang, Z. Zhao, G. Huang, B. S. Li and B. Z. Tang, A versatile tetraphenylethene derivative bearing excitation wavelength dependent emission, multistate mechanochromism, reversible photochromism, and circularly polarized luminescence and its applications in multimodal anticounterfeiting, *CCS Chem.*, 2023, **5**, 1663–1673.
35 R. Liang, G. Dong, J. Tian, S. Gao, Y. Yang, B. Wang and X. Li, Study on mechanofluorochromism, ink-free writing, and latent fingerprint imaging of the functionalized difluoroboron compounds with methyl and methoxy, *Opt. Mater.*, 2024, **156**, 115991.
36 A. Afrin and P. C. A. Swamy, Symphony of light: AIE and MFC in carbazole-based cyanostilbenes, *J. Mater. Chem. C*, 2024, **12**, 1923–1944.
37 A. Afrin and P. C. A. Swamy, Tailoring Emission Color shifts in Mechanofluorochromic Active AIE Systems of Carbazole-Based D-π-A conjugates: Impact of π Spacer Unit Variants, *J. Org. Chem.*, 2024, **89**, 7946–7961.
38 A. Afrin and P. C. A. Swamy, π-Spacer Engineering: Driving Near-infrared Aggregation Induced-emission and Mechanofluorochromism in Carbazole-biscyanostilbenes, *Chem. – Eur. J.*, 2024, e202403644.
39 A. Afrin and P. C. A. Swamy, Structural modulations: unraveling the impact of benzothiazole positions on the optical properties of carbazole–cyanostilbenes, *CrystEngComm*, 2025, **27**, 3664.
40 L. Zhu and Y. Zhao, Cyanostilbene-based intelligent organic optoelectronic materials, *J. Mater. Chem. C*, 2013, **1**, 1059–1065.
41 A. Afrin and P. C. A. Swamy, Aggregation induced emission and reversible mechanofluorochromism active carbazole–anthracene conjugated cyanostilbenes with different terminal substitutions, *New J. Chem.*, 2023, **47**, 18919–18932.
42 C. Femina, M. Shanthil, P. K. Sajith and R. Thomas, Anthracene-incorporated cyanostilbene based donor–acceptor systems: intramolecular charge transfer and aggregation induced emission, *New J. Chem.*, 2023, **47**, 13810–13819.
43 A. Afrin and P. C. A. Swamy, *Inorg. Chem.*, 2025, **64**(34), 17459–17469.
44 O. Anitha, M. Mathivanan, B. Tharmalingam, T. Thiruppathiraja, S. Ghorai, R. Natarajan, V. Thiagarajan, S. Lakshmipathi and B. Murugesapandian, Multi-stimuli responsiveness of pyrimidine bishydrazone: AIE, tuneable luminescence, white light emission, mechanochromism, acidochromism and its anticounterfeiting applications, *Dyes Pigm.*, 2023, **212**, 111091.
45 Z. Zhao, H. Zhang, J. W. Y. Lam and B. Z. Tang, Aggregation-induced emission: new vistas at the aggregate level, *Angew. Chem., Int. Ed.*, 2020, **59**, 9888–9907.
46 M. J. Frisch, G. W. Trucks, H. B. Schlegel, G. E. Scuseria, M. A. Robb, J. R. Cheeseman, G. Scalmani, V. Barone, G. A. Petersson, H. Nakatsuji, X. Li, M. Caricato, A. V. Marenich, J. Bloino, B. G. Janesko, R. Gomperts, B. Mennucci, H. P. Hratchian, J. V. Ortiz, A. F. Izmaylov, J. L. Sonnenberg, D. Williams-Young, F. Ding, F. Lipparini, F. Egidi, J. Goings, B. Peng, A. Petrone, T. Henderson, D. Ranasinghe, V. G. Zakrzewski, J. Gao, N. Rega, G. Zheng, W. Liang, M. Hada, M. Ehara, K. Toyota, R. Fukuda, J. Hasegawa, M. Ishida, T. Nakajima, Y. Honda, O. Kitao, H. Nakai, T. Vreven, K. Throssell, J. A. Montgomery Jr., J. E. Peralta, F. Ogliaro, M. J. Overo Bearpark, J. J. Heyd, E. N. Brothers, K. N. Kudin, V. N. Star v, T. A. Keith, R. Kobayashi, J. Normand, K. Raghavachari, A. P. Rendell, J. C. Burant, S. S. Iyengar, J. Tomasi, M. Cossi, J. M. Millam, M. Klene, C. Adamo, R. Cammi, J. W. Ochterski, R. L. Martin, K. Morokuma, O. Farkas, J. B. Foresman and D. J. Fox, *Gaussian 09, Revision B.01*, Gaussian, Inc., Wallingford, CT, 2016.
47 M. Hosseinnezhad, S. Nasiri, V. Nutalapati, K. Gharanjig and A. M. Arabi, A review of the application of organic dyes based on naphthalimide in optical and electrical devices, *Prog. Color, Color. Coat.*, 2024, **17**, 417–433.
48 CCDC 2500771: Experimental Crystal Structure Determination, 2025, DOI: 10.5517/ccdc.csd.cc2py81z.